JACS
JOURNAL OF THE AMERICAN CHEMICAL SOCIETY
pubs.acs.org/JACS
Article

Geometric Transformations Afforded by Rotational Freedom in Aramid Amphiphile Nanostructures

Yukio Cho, Yu-Jin Choi, Samuel J. Kaser, Rebecca Meacham, Ty Christoff-Tempesta, Siyu Wu, Xiaobing Zuo, and Julia H. Ortony*

Cite This: J. Am. Chem. Soc. 2023, 145, 22954−22963
Read Online

ABSTRACT: Molecular self-assembly in water leads to nanostructure geometries that can be tuned owing to the highly dynamic nature of amphiphiles. There is growing interest in strongly interacting amphiphiles with suppressed dynamics, as they exhibit ultrastability in extreme environments. However, such amphiphiles tend to assume a limited range of geometries upon self-assembly due to the specific spatial packing induced by their strong intermolecular interactions. To overcome this limitation while maintaining structural robustness, we incorporate rotational freedom into the aramid amphiphile molecular design by introducing a diacetylene moiety between two aramid units, resulting in diacetylene aramid amphiphiles (D-AAs). This design strategy enables rotations along the carbon−carbon *sp* hybridized bonds of an otherwise fixed aramid domain. We show that varying concentrations and equilibration temperatures of D-AA in water lead to self-assembly into four different nanoribbon geometries: short, extended, helical, and twisted nanoribbons, all while maintaining robust structure with thermodynamic stability. We use advanced microscopy, X-ray scattering, spectroscopic techniques, and two-dimensional (2D) NMR to understand the relationship between conformational freedom within strongly interacting amphiphiles and their self-assembly pathways.

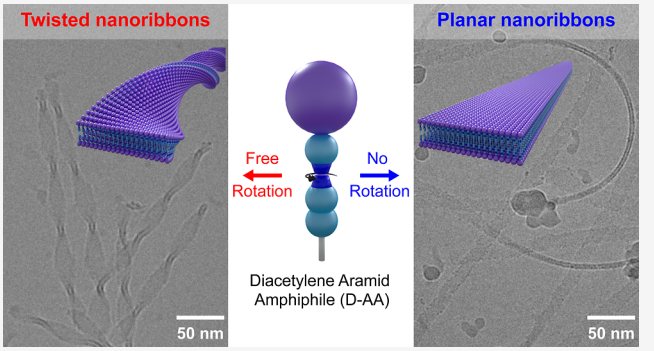

INTRODUCTION

Molecular self-assembly plays a critical role in forming diverse supramolecular architectures and functional macromolecules in biological systems, such as cell membranes and protein structures.[1−3] These assemblies are dominated by noncovalent interactions, and their dynamic nature often results in nanostructures with diverse and tunable morphologies. This diversity is key to complex cellular processes.[4] Synthetic amphiphiles self-assemble in a similar manner and offer a bottom-up approach to constructing nanostructures with programable functionalities and pristine arrangements.[5−7] Examples of self-assembling synthetic amphiphiles include peptide amphiphiles,[8,9] chromophore amphiphiles,[10,11] and lipids.[12,13] These assemblies have high surface areas and are dynamic within the nanostructures,[14,15] making them promising for applications that mediate reactions and require responsiveness.[16−18] The ability to control nanostructure morphology through molecular design and environmental conditions is important for achieving the desired functions for targeted applications. For example, peptide amphiphile nanofibers serve as tissue scaffolds for cell repair and regeneration,[19] lipid-based liposomes and self-assembled nanoparticles facilitate drug delivery,[20] and nanotubes self-assembled from rigid-flexible block amphiphiles function as supramolecular channel reactors.[21]

Strongly interacting amphiphiles, which exhibit robust intermolecular interactions upon self-assembly, have emerged as a unique class of self-assembling molecular building blocks. These supramolecular nanostructures possess high mechanical stabilities due to their strong intermolecular forces[14,22] and have been reported for applications in electrical,[23,24] optical,[25−27] and water remediation.[28] However, these amphiphiles are generally fixed into specific conformations during assembly since strong intermolecular interactions are directional.[29] This constraint often limits the range of morphologies achievable by nanostructures composed of strongly interacting amphiphiles. Therefore, we hypothesize that building rotational freedom into the molecular design of strongly interacting amphiphiles will allow us to harness both

Received: May 3, 2023
Published: October 11, 2023

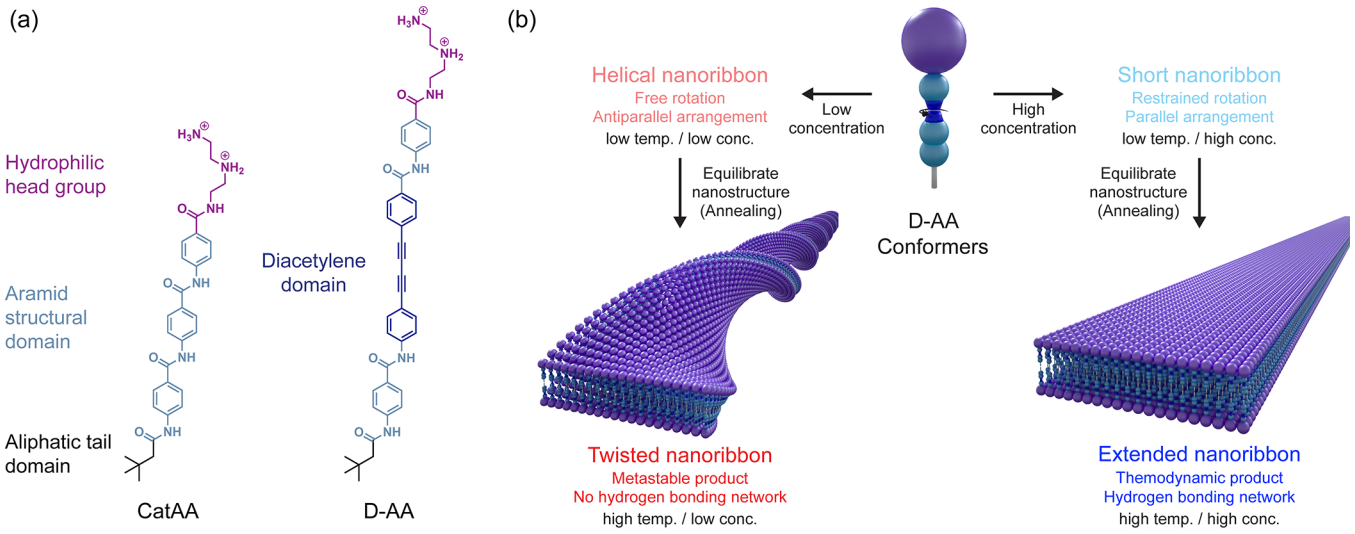

Figure 1. AAs with rotational domain exhibit polymorphism in self-assembled nanostructures. (a) AAs contain a hydrophilic headgroup (purple), an aramid structural domain (cyan), and an aliphatic tail domain (black). AAs with the cationic headgroup and diacetylene domain (blue) are synthesized in this study (D-AAs), and previously reported CatAAs without the diacetylene domain are used as a control.[22] (b) D-AAs exhibit four different self-assembled nanostructures in water by varying thermal equilibration temperature (high or low temp.) and initial concentrations (high or low conc.), which are helical, twisted, short planar, and extended planar nanoribbons.

structural robustness and will facilitate a diversity of supramolecular geometries.

Aramid amphiphiles (AAs) are a class of strongly interacting amphiphiles that self-assemble to form high aspect ratio nanoribbons with robust mechanical properties and suppressed dynamic motion.[14] AAs contain a hydrophilic headgroup and an aliphatic tail, similar to phospholipids, but also incorporate a "structural domain" consisting of usually three aromatic amides (aramids) (Figure 1a). The structural domain provides strong intermolecular cohesion via collective hydrogen bonding and $\pi-\pi$ stacking interactions. AAs, similar to other strongly interacting amphiphiles, are limited in their range of achievable morphologies.[30,31] Therefore, AAs provide a platform for investigating the role of rotational freedom within each molecule.

In this study, we incorporate a diacetylene domain into the molecular design of an AA molecule (D-AA) for two reasons: (1) to promote rotational freedom only along the carbon−carbon sp hybridized bond within the aramid structural domain, and (2) because the diacetylene domain within a nanostructure serves as a fluorescent probe (Figure 1a). Introducing conformational flexibility into the backbone of self-assembling amphiphiles typically results in a variety of packing motifs and leads to multiple simultaneous nanostructure geometries after self-assembly.[31] Such a diversity of nanostructures makes it challenging to identify relationships between amphiphile features and nanostructure geometry.[32] In this study, we designed D-AAs with a single-axis rotational freedom in order to permit only rotation freedom in one direction of the molecule. This constrained motion allows us to probe how the molecular conformation impacts the self-assembly pathways. Additionally, the fluorescent nature of the D-AA nanostructures will allow us to investigate conformational changes and intermolecular interactions with domain-specificity of different supramolecular morphologies.[33]

RESULTS AND DISCUSSION

We synthesized D-AAs by incorporating the diacetylene domain into the previously reported molecular design of a cationic AA, CatAA (Figure 1a).[14] Synthesis details and characterization of the D-AAs and their intermediates are provided in the Supporting Information (Figures S1−S12). The self-assembly of CatAAs consistently forms high aspect ratio planar nanoribbons, independent of the wide range of initial concentrations and thermal equilibration temperatures.[14] However, changes in pH conditions can influence this due to the positively charged surface chemistry.[31] In this study, we maintain the same hydrophilic headgroup of two AAs in order to eliminate any morphological changes that may be related to the headgroup chemistry. Unlike the assembly of CatAAs, the assembly of D-AAs in water shows explicit dependence on the concentration and temperature by conventional transmission electron microscopy (TEM) and cryogenic TEM (cryo-TEM) (Figure 1b). More specifically, we discover that D-AAs self-assemble into helical nanoribbons at a low concentration and room temperature in water (Figure 2a and S13), and a morphological transition occurs from helical to twisted nanoribbons after equilibrating the assemblies at elevated temperatures for 24 h (Figure 2b). The population of twisted nanoribbons increases with increasing annealing temperature from 40 °C (Figure S14) to 60 °C (Figure S15), and by 75 °C, the D-AA nanostructures completely transition into twisted nanoribbons (Figure S16). Meanwhile, we confirm the D-AA molecules maintain their original molecular weight after annealing, indicating the diacetylene domain of D-AA is thermally stable in water at these elevated temperatures (Figure S12). Based on cryo-TEM, the widths of helical nanoribbons and the thickness of twisted nanoribbons are 4.6 and 5.2 nm, respectively. We further find that the radius and pitch length of helical nanoribbons are variable in both the TEM and cryo-TEM images, indicating no intermolecular forces to stabilize the helical nanostructure between the surfaces. In contrast, the nanoribbon length, width, and pitch length of twisted nanoribbons increase with increasing

https://doi.org/10.1021/jacs.3c04598
J. Am. Chem. Soc. 2023, 145, 22954−22963

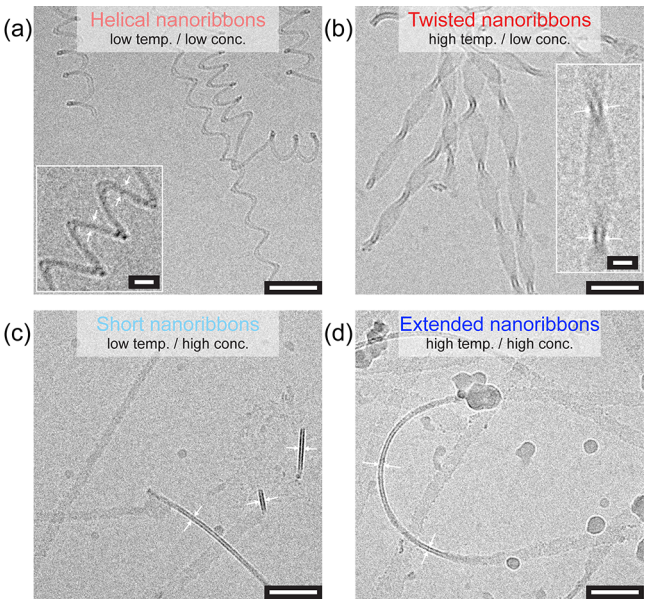

Figure 2. Representative cryo-TEM images of four different D-AA nanostructures self-assembled in water at various initial concentrations and thermal equilibration temperatures. White arrows indicate ribbon dimensions. (a) Helical nanoribbons with a 4.6 nm ribbon width formed at 20 °C with 1 mg/mL concentration (low temp./low conc.), (b) twisted nanoribbons with a 5.2 nm ribbon thickness formed at 75 °C with 1 mg/mL concentration (high temp./low conc.), (c) short planar nanoribbons with a 5.2 nm ribbon thickness formed at 20 °C with 10 mg/mL concentration (low temp./high conc.), and (d) extended planar nanoribbons with a 5.2 nm ribbon thickness formed at 75 °C with 10 mg/mL concentration (high temp./high conc.). (Scale bar, 50 nm; inset scale bar, 10 nm).

annealing temperatures (Figures S19 and S20). These morphological features are preserved at room temperature for an extended period and are unaffected by dilution. This stability suggests that each D-AA twisted nanoribbon represents a thermodynamically metastable state and becomes deeply kinetically trapped upon self-assembly. A sublinear scaling relationship of width and pitch length indicates that the deformation energy is not simply proportional to the average curvature of the entire nanostructure (Figure S20).[34] Notably, such chiral nanostructures are first observed in these D-AA assemblies among the collections of self-assembling AA nanostructures. At higher initial concentrations, D-AAs self-assemble into short planar nanoribbons at room temperature in water (Figure 2c and S17), and the average length of the planar nanoribbons is extended after equilibrating the assemblies at elevated temperatures for 24 h (Figure 2d and S18). Both planar nanoribbons have a thickness of 5.2 nm and variable widths, calculated from cryo-TEM images.

Small-angle X-ray scattering (SAXS) was carried out to evaluate the nanostructure morphologies quantitatively. SAXS profiles of the four D-AA nanostructures present a slope of −2 in the low-q regime, suggesting that all D-AA assemblies behave as one-dimensional nanostructures in the solution (Figure 3a).[35] For extended planar, short planar, and twisted nanoribbons, the SAXS profiles best fit a lamellar bilayer model with a thickness of 5.0, 4.8, and 5.0 nm, respectively (Figures S21−S23).[36] These fits corroborate the thicknesses measured by cryo-TEM and previously reported fits for CatAA nanoribbons.[30] Wide-angle X-ray scattering (WAXS) provides insights into long-range ordering and molecular organization. WAXS profiles of extended and short planar nanoribbons show a characteristic peak of uniform intermolecular distances (d = 4.93 Å), whereas the profiles of helical and twisted nanoribbons do not contain information about long-range molecular packing (Figure 3b). These uniform intermolecular distances represent an extended hydrogen bonding network along the nanoribbons, which has been confirmed in other self-assembling AA nanostructures.[22] Based on the X-ray scattering results, we speculate that the hydrogen bonding network among aramid domains of D-AAs is activated only at high concentrations. When the concentration is low, the D-AAs are packed in a distinct way. This new packing preference likely leads to the formation of chiral structures, such as helical and twisted nanoribbons, in D-AA assemblies. Absorption spectroscopy is commonly used in supramolecular chemistry to identify changes in conformation and secondary bonding for chromophores.[37,38] Compared to the UV−visible absorption spectrum of CatAA nanoribbon suspensions, which only shows a single peak at 298 nm,[22] the absorption spectra of the D-AA nanostructure suspension exhibit three local maxima due to the addition of the diacetylene moiety (Figure 3c). The D-AA helical and twisted nanoribbons share virtually identical local maxima at 322, 342, and 370 nm. The peaks for twisted nanoribbons possibly have more defined shapes, likely because of the optimization of molecular arrangement at the elevated temperature. This molecular rearrangement is also probed by site-directed spin-labeling and electron paramagnetic resonance (SDSL-EPR) spectroscopy, a technique used to investigate conformational dynamics within specific domains.[39] The SDSL-EPR spectra suggest that the ejection of spin-labeled AAs occurs during the morphological transition of D-AA helical into twisted nanoribbons (Figure S24).

At high concentrations and without thermal equilibration, we observe a subtle bathochromic (red) shift between helical and short planar nanoribbons. In contrast, moving from short to extended planar nanoribbons, a larger and systematic bathochromic shift ($\Delta\lambda$ = 17 nm) occurs for all three local maxima after equilibration at the elevated temperature. In addition to the systematic bathochromic shift from thermally equilibrated samples, we also notice that the peak at the low wavelength becomes relatively weaker and the peaks at high wavelengths become relatively stronger with increasing the concentration of D-AAs gradually (Figure S25). Previously, we confirmed that a bathochromic shift indicates a reduced intermolecular interaction for self-assembled AA nanostructures.[31,40] However, we also confirmed from solution WAXS that the hydrogen bonding network among D-AAs is activated when bathochromic shifts occur at high concentrations (Figure 3b). Hence, we consider that the different packing preference at low and high concentrations is caused by the conformational changes of D-AA, which lead to the shifts and changes in the UV−vis spectra's peak ratios. The conformational difference between morphologies is further supported by Fourier-transform infrared (FT-IR) spectroscopy. At low concentrations, we observe a shift in the carbonyl (C═O) amide I stretch peaks as the annealing time extends (Figure 3d). Conversely, at high concentrations, the C═O amide I stretch peaks at 1656 and 1642 cm^{-1} become more pronounced as the annealing time increases, but without shifting, suggesting the formation of a collective hydrogen bonding network (Figure 3e). The peaks at 1672 and 1600 cm^{-1} are assigned to carbonyl stretching of the amide bond connecting the headgroup to the aramid structural domain and carbon−carbon stretching in the

https://doi.org/10.1021/jacs.3c04598
J. Am. Chem. Soc. 2023, 145, 22954−22963

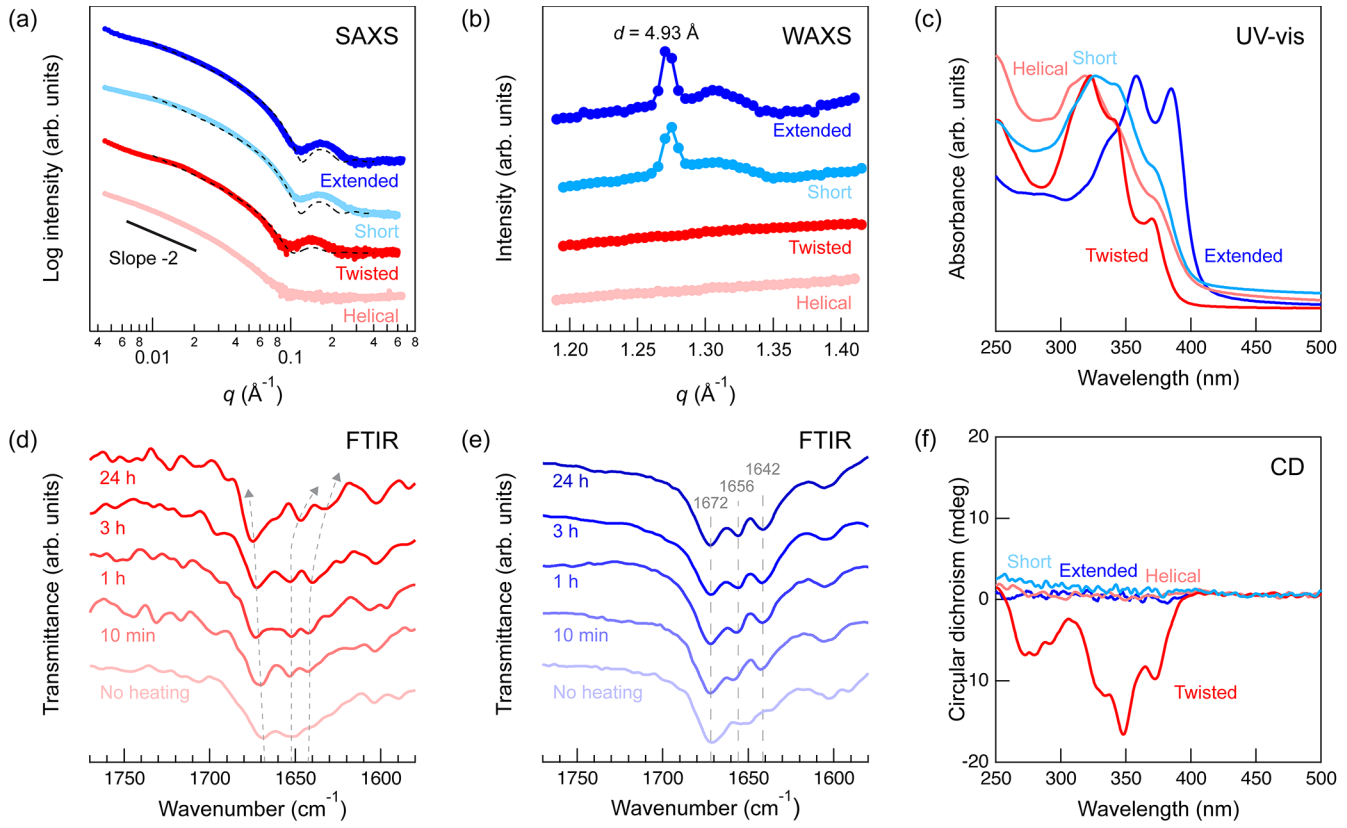

Figure 3. SAXS, UV−vis, FT-IR, and circular dichroism (CD) spectroscopy reveal the morphological, structural, and conformational differences of D-AA nanostructures. (a) SAXS of D-AA nanostructures in water indicates a slope of −2 in the low-q regime, indicating one-dimensional nanostructures, and best fits the lamellar model (black dotted), yielding a 4.8−5.0 nm thickness. (b) WAXS of D-AA extended and short nanoribbons (blue and cyan) show a characteristic peak of the uniform intermolecular distances (d = 4.93 Å), which indicates an extended hydrogen bonding network. (c) Normalized UV−vis absorption spectra of D-AA nanostructures reveal differences arising from molecular conformation and packing of D-AAs in the nanostructures. Time-dependent ATR−FTIR spectra for D-AAs at concentrations of (d) 1 mg/mL and (e) 10 mg/mL in D_2O, annealed at 75 °C, reveal clear differences in the conformational state of D-AAs between twisted (low conc) and extended planar (high conc.) nanoribbons. The gray dashed lines visually indicate the trend of transition in the peak positions. (f) CD spectrum of D-AA twisted nanoribbons (red) displays a negative signal induced by twist, spanning the range of 250−400 nm, whereas the CD spectra of other D-AA nanostructures exhibit no optical activity.

aromatic units, respectively. This contrast in the time-dependence of the FT-IR spectra during annealing further suggests a dependence of the preferred intermolecular interactions and conformational states of D-AA self-assembly on the concentration of D-AAs. The FT-IR spectra of the powdered samples, obtained from freeze-drying the suspension of D-AA nanostructures, further exhibit an intensified peak at 1593 cm^{-1} for D-AA short and extended planar nanoribbons (high concentration) when compared to both the CatAA control nanoribbons and D-AA helical and twisted nanoribbons (low concentration) (Figure S26). This peak is associated with the typical ring deformation of the aryl group adjacent to the diacetylene domain.[41,42] These results suggest that alterations in the average electronic environment of the aryl groups adjacent to the diacetylene domain occur between different morphologies.

Interestingly, CD reveals that only twisted nanoribbons of D-AA exhibit optically active spectra, while the other three D-AA nanostructures do not have detectable CD signals (Figure 3f). We confirm by measuring the spectra of D-AA fully dissolved in dimethyl sulfoxide (DMSO) that the achiral D-AA shows no CD signal (Figure S27). We also measured the CD spectrum of CatAA to confirm that the aramid structural domain does not contribute to the optical activity (Figure S27). Therefore, the observed optical activity of D-AA twisted nanoribbons is unique to that particular nanostructure and is unexpected. We analyzed the CD spectrum of 60 independently prepared samples of D-AA twisted nanoribbons and found a negative, left-handed chiral signature in every sample (Figure S28). We then analyzed the extent of nanostructure chirality by plotting the ratio between the CD intensity and UV−vis absorption intensity of D-AA twisted nanoribbons. This ratio yields the anisotropy, or dissymmetry g-factor (Figure S29). The g-factor is given by the equation $g = \Delta\varepsilon/\varepsilon$, where $\Delta\varepsilon$ is the molar CD intensity and ε is the molar extinction coefficient. The calculated wavelength-dependent g-factor maximum is found to be 2.5×10^{-4} at 350 nm for D-AA twisted nanoribbons. This value is comparable to the typical g-factor range (10^{-3} to 10^{-5}) of optically active materials.[43,44]

The origin of the uniform left-handedness observed in D-AA twisted nanoribbons is unknown but may be explained by trace levels of organic substances present in the ambient environment acting as chiral inductors. Despite their seemingly negligible concentration, these substances with chiral centers may serve as self-assembly precursors, favoring the left-handed growth of D-AA twisted nanoribbons. By utilizing linear dichroism, we have also eliminated the possibility that the optical activity of D-AA twisted nanoribbons is a result of the

https://doi.org/10.1021/jacs.3c04598
J. Am. Chem. Soc. 2023, 145, 22954−22963

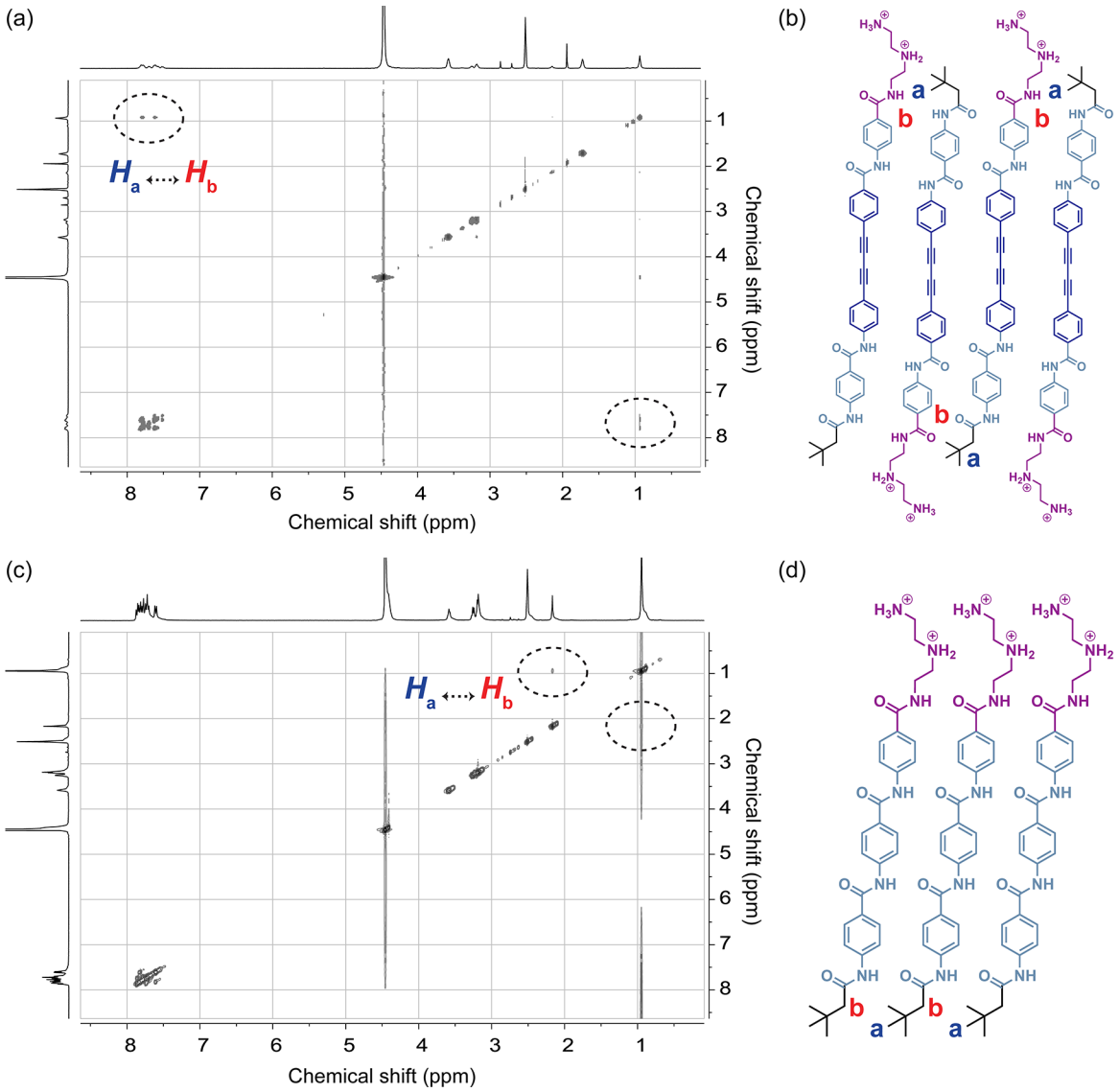

Figure 4. 2D NOESY NMR spectra of D-AAs and CatAAs exhibit their distinct intermolecular interactions in the nanostructures. (a) 2D NOESY of D-AAs shows off-diagonal cross peaks between the aromatic ring and methylene group protons of aramid structural and aliphatic tail domains, indicating that these two domains are close in space. (b) Proposed antiparallel arrangement of D-AAs leads to the formation of helical and twisted nanoribbons at diluted concentrations. (c) 2D NOESY of CatAAs only shows short-range off-diagonal cross peaks between hydrogen atoms in aliphatic tail domains. (d) Proposed parallel arrangement of CatAAs promotes the formation of collective hydrogen bonding and only allows CatAAs to self-assemble into high aspect ratio nanoribbons. The protons of H_a and H_b peaks from a and c are marked in b and d. All samples were prepared in a 70:30 mixture of D_2O and DMSO-d_6.

partially linear alignment of assemblies (Figure S30).[45] Notably, very few studies have reported the formation of optically active supramolecular nanostructures with uniform handedness, assembled from achiral small molecules.[46,47] Further investigations are necessary to understand the cause of the uniform left-handedness in twisted nanoribbons of D-AA.

Further experiments were conducted to deepen our understanding of the relationship between nanostructure geometries, packing preference, and conformational changes in D-AA assemblies. To relate packing preference to different morphologies, two-dimensional NMR spectroscopy was carried out to investigate the intermolecular proximity of ^{1}H sites between D-AAs in water.[48,49] Since NMR requires a high concentration of compounds to obtain substantial signals but self-assembly of the D-AA nanostructures is sensitive to the initial concentration, a solution of 3:7 DMSO-d_6/D_2O is used to simulate the intermolecular interaction of the fully dissolved D-AAs. Through TEM and solution WAXS, we confirm that neither CatAAs nor D-AAs in this solution form any nanostructures or a hydrogen bonding network. The analogous UV−vis spectra indicate that the D-AAs in this solution represent the interactions in D-AA helical and twisted nanoribbons self-assembled at a low concentration (Figure S31). Two-dimensional nuclear Overhauser effect spectroscopy (2D NOESY) of D-AAs in the solution reveals off-diagonal cross peaks between the aromatic ring and methylene group protons of the aramid structural and aliphatic tail domains (Figure 4a). These off-diagonal cross peaks confirm that the aramid structural and aliphatic tail domains of D-AAs are spatially close and are packed in an antiparallel arrangement during self-assembly at low concentrations (Figure 4b). In

https://doi.org/10.1021/jacs.3c04598
J. Am. Chem. Soc. 2023, 145, 22954−22963

contrast, the 2D NOESY of CatAAs in the solution shows short-range off-diagonal cross peaks in a different position, which are attributed to the hydrogen atoms in aliphatic domains (Figure 4c). This 2D NOESY result verifies that the CatAAs are arranged in a parallel manner to promote the formation of a collective hydrogen bonding network (Figure 4d), corroborating with the previously reported molecular crystalline structure.[14] We further confirmed that these off-diagonal cross peaks of D-AAs and CatAAs in 2D NOESY are absent in two-dimensional total correlation spectroscopy (2D TOCSY), which yields the correlation about the intramolecular interaction of protons in an unbroken chain of coupled spins (Figure S32).

Meanwhile, diffraction analyses of cryo-TEM images and WAXS patterns of dried nanoribbon thread reveal that the molecular packing of D-AA short and extended planar nanoribbons resembles the arrangement in CatAA nanoribbons. A magnified view of the cryo-TEM image of a D-AA extended nanoribbon shows periodically repeating contrasts with a plane-to-plane distance of 5.0 Å (Figure 5a). The fast Fourier transform (FFT) operation of the cryo-TEM image yields a clear diffraction pattern (Figure 5b), and this FFT image fits the uniform intermolecular distances of 5.0 Å along

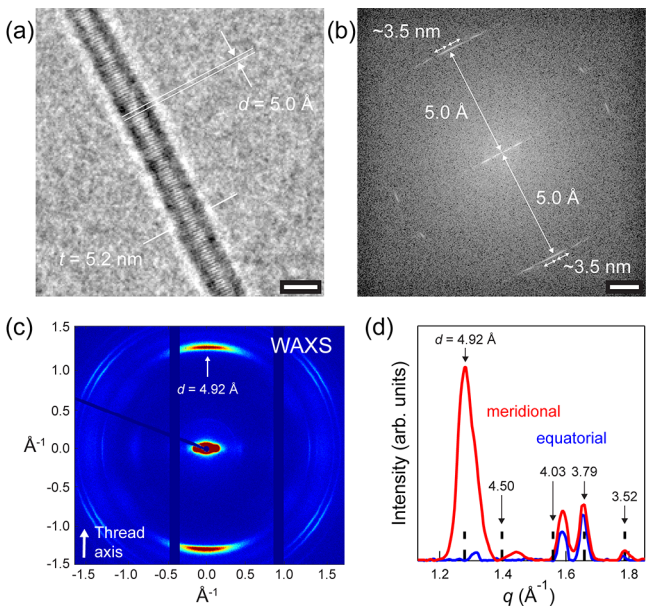

Figure 5. D-AA extended and short nanoribbons display organized molecular packing and an extended hydrogen bonding network in the solution and after being processed to solid-state nanoribbon threads. (a) Zoomed-in cryo-TEM image of the D-AA extended nanoribbon shows a 5.2 nm thickness of the nanoribbon and explicit, long-range ordered distances of 5.0 Å (scale bar, 5 nm). (b) FFT image of a shows two clear diffraction peaks corresponding to the uniform intermolecular distances (d = 5.0 Å) and indicates the thickness of the diffraction region in the nanoribbons is ~3.5 nm, which is contributed from the length of aramid structural and diacetylene domains (scale bar, 2 nm^{-1}). (c) WAXS pattern of a D-AA extended nanoribbon thread shows analogous molecular organization in the solid-state thread as previously reported in the CatAA nanoribbon thread.[14] (d) One-dimensional scattering profile is obtained by integrating the meridional and equatorial axes of c. Black dotted lines represent simulated peak positions of a unit cell with a = 7.04 Å, b = 4.92 Å, and c = 11.15 Å, and space group 26: $Pmc2_1$ based on poly(p-benzamide), reported in the previous study.[14]

the nanoribbon and a 3.5 nm thickness of the diffraction region in the nanoribbons, which is shorter than the entire thickness of the nanoribbon (Figure S33). This fitting is consistent with the previous solution WAXS results (Figure 3b). The ~5.0 Å uniform intermolecular distances represent an extended hydrogen bonding network along the nanoribbons, implying a parallel arrangement of D-AAs in the extended planar nanoribbons. A shorter thickness of the diffraction region is likely due to the absence of diffraction within the flexible hydrophilic headgroup domain. The periodically repeating contrasts and clear diffraction patterns are confirmed in both D-AA extended and short planar nanoribbons at multiple angles and curvatures, indicating that the contrasts are not due to the artificial effects of cryo-TEM imaging (Figures S34 and S35).

A unique capability of the AA platform is the formation of flexible and stable solid-state threads by shear alignment in a divalent salt solution due to the nanostructures' stability and high aspect ratio (Figure S36). WAXS patterns of the dried nanoribbon thread in a vacuum allow us to confirm molecular crystalline structures and study the molecular arrangement within the nanoribbons.[14] However, the preparation of these solid-state threads requires long and straight nanostructures, and thus WAXS of only the extended nanoribbon morphologies are studied. A WAXS pattern of a D-AA extended nanoribbon thread presents the most substantial WAXS peaks at a d-spacing of 4.92 Å along the thread axis (Figure 5c), corroborating with the previous solution WAXS profiles (Figure 3b) and cryo-TEM image (Figure 5a). These anisotropic WAXS peaks have a pattern identical to that of the previously reported CatAA nanoribbon thread, implying an analogous molecular organization between D-AA extended and CatAA nanoribbons. Integrating the meridional and equatorial axes of the WAXS pattern yields a one-dimensional scattering profile. These peaks fit the same simulated unit cell previously used for fitting CatAA nanoribbon threads (Figure 5d). A subtly decreased intermolecular distance and increased nanoribbon thickness for the D-AA extended nanoribbon thread can likely be attributed to the addition of the diacetylene domain. Combining the results of 2D NMR, cryo-TEM images, and WAXS patterns, we reveal that the self-assembly of D-AAs favors antiparallel or parallel molecular packing at low or high concentrations, respectively.

Therefore, we hypothesize that the relationship among nanostructure geometries, packing preference, and conformational changes in D-AA assemblies can be explained as follows: When the D-AA concentration is low, the rotational freedom of the diacetylene domain leads D-AAs to a torsional state that prefers antiparallel molecular packing. This antiparallel arrangement of D-AA assemblies sterically hinders hydrogen bonding between aramid domains and induces transformation into helical nanoribbons. This torsional state guides the self-assembly of D-AAs into helical nanoribbons. Compared to the control CatAA, the incorporated rotational freedom of D-AAs likely alters the temperature dependence of self-assembly pathways due to an additional entropy cost associated with self-assembly. However, the antiparallel arrangement serves a metastable state, and the thermal energy is insufficient to overcome the intermolecular cohesion and change the arrangement. Thus, D-AAs self-assemble into twisted nanoribbons at low concentrations and elevated temperatures rather than forming planar nanoribbons. On the contrary, a stronger driving force of amphiphilic self-assembly restrains the

https://doi.org/10.1021/jacs.3c04598
J. Am. Chem. Soc. 2023, 145, 22954−22963

rotational freedom of D-AAs and promotes the parallel molecular packing during the self-assembly when the D-AA's concentration is high. This parallel packing activates the collective hydrogen bonding between aramid domains and induces the self-assembly of planar nanoribbons. The hydrogen bonding network is further extended to form D-AA extended planar nanoribbons after equilibration at the elevated temperature.

Fluorescence spectra of D-AA nanostructures further support our model of the conformational changes and intermolecular interactions of diacetylene moieties within the aramid structure domains. At the ppm-order concentrations, the luminescent quantum yield Φ_f of D-AAs is determined to be 0.02% (Figure S37). Each of the four different nanostructures of D-AA assemblies shows subtle shifts of the excitation and emission maxima, with increased emission intensities for D-AA short and extended planar nanoribbons (Figure 6). The excitation wavelength ($\lambda_{Exc.}$) and emission

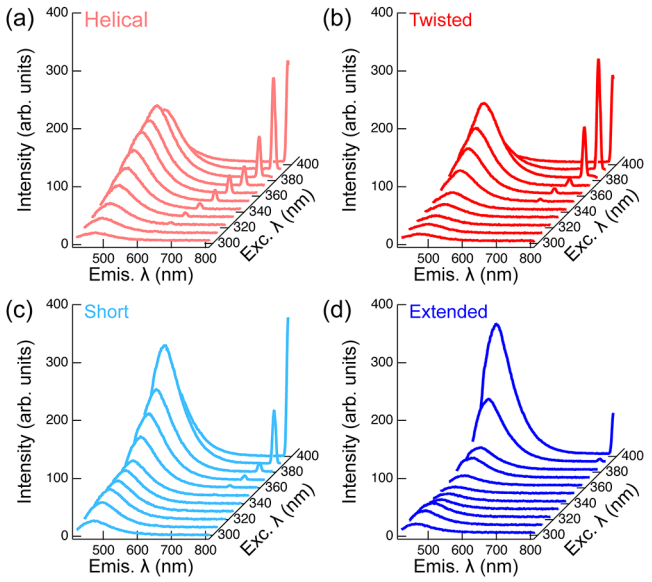

Figure 6. 3D fluorescence spectra of four different D-AA nanostructures self-assembled in water at various initial concentrations and thermal equilibration temperatures. (a) Helical nanoribbons formed at 20 °C with 1 mg/mL concentration, (b) twisted nanoribbons formed at 75 °C with 1 mg/mL concentration, (c) short planar nanoribbons formed at 20 °C with 10 mg/mL concentration, and (d) extended planar nanoribbons formed at 75 °C with 10 mg/mL concentration. The sharp peaks that emerge at doubled wavelengths of excitation light are attributed to second-order Rayleigh scattering from the D-AA nanostructures. The concentration of all D-AA nanostructures for the fluorescence measurement is normalized at 0.1 mg/mL.

wavelength ($\lambda_{Emis.}$) where D-AA nanostructures exhibit a maximum emission intensity are obtained by refined scans (Figure S38), and the results with their corresponding energy are summarized in Table 1. We observe that D-AA nanostructures with parallel molecular packing (short and extended) show insignificantly longer $\lambda_{Exc.}$ and shorter $\lambda_{Emis.}$ than those with antiparallel molecular packing (helical and twisted). Coulomb interactions between fluorophores can lead to spectral shifts in fluorescence, especially between parallel and antiparallel molecular arrangements. However, in this case, the energy differences (5−10 kJ/mol) are too subtle compared

Table 1. Maximum Excitation Wavelength ($\lambda_{Exc.}$), Emission Wavelength ($\lambda_{Emis.}$) and Their Corresponding Energy of D-AA Nanostructures

Nanostructures	$\lambda_{Exc.}$ (nm)	Energy of $\lambda_{Exc.}$ (kJ/mol)	$\lambda_{Emis.}$ (nm)	Energy of $\lambda_{Emis.}$ (kJ/mol)
Helical	381	314.3	463	258.6
Twisted	379	315.9	470	254.8
Short	391	306.2	459	260.9
Extended	399	300.1	460	260.3

to the typical spectral shifts reported in coulomb coupling differences, such as shifts between H- and J-aggregation.[50,51] Indeed, this energy difference is the same magnitude as that of the different torsional states of D-AAs with and without rotational freedom.[52−54] The restricted rotational freedom of the diacetylene domain can also explain the increased emission intensities for parallel molecular arrangements.[55] Notably, we confirm that the D-AA assemblies are fluorescent also in the solid-state after drying from the solution, indicating no aggregation-caused quenching occurs (Figure S39). These results suggest that the fluorescence of D-AAs is preserved in the solid-state through self-assembly, which demonstrates an alternative approach to developing fluorescent materials in both solution and solid-state for optoelectronic devices, imaging agents, and biosensors.[56]

CONCLUSIONS

In summary, we have presented four different nanostructure geometries of D-AA assemblies in water by varying the initial concentrations of amphiphiles and the thermal equilibration temperatures. When the initial concentration of D-AAs in water is low (≈1 mg/mL), helical nanoribbons are favored for self-assembly at room temperature. These helical nanostructures can be further equilibrated at elevated temperatures, at which point the helices transform into twisted nanoribbons. When D-AA nanostructures are in the twisted ribbon morphology, they exhibit a negative CD signal, corresponding to solely left-handed chirality. This D-AA nanostructure is the only type among all of the AA nanostructures to exhibit chiral properties so far. We conducted 2D NOESY to characterize the molecular packing within twisted nanoribbons and show that unlike other AA assemblies, the chiral twisted ribbons assume an antiparallel packing arrangement. However, the origin of the uniform left-handedness of D-AA twisted nanoribbons is still unknown and requires further investigation for a comprehensive understanding.

In contrast to the low-concentration assemblies, we find that at high concentrations (≈10 mg/mL), the D-AAs self-assemble into planar nanoribbons with collective hydrogen bonding networks, similar to other AAs. This long-range ordering of the hydrogen bonding network along the nanoribbon long-axis is confirmed by solution WAXS, diffraction analysis of cryo-TEM images, and WAXS patterns of aligned dried nanoribbons (threads). WAXS patterns of the aligned threads further show that D-AA extended planar nanoribbons have a molecular organization similar to that of CatAA nanoribbons, suggesting that the D-AA packs in a parallel arrangement at high concentrations. This parallel molecular arrangement is caused by the stronger driving force of amphiphilic self-assembly, which restrains the rotational freedom of D-AAs.

Among the four different nanostructures, the fluorescence spectra exhibit subtle shifts in the emission and excitation

https://doi.org/10.1021/jacs.3c04598
J. Am. Chem. Soc. 2023, 145, 22954−22963

maxima. These shifts correspond to a small energy difference (5−10 kJ/mol), which is likely caused by the different torsional states of D-AAs with and without rotational freedom rather than from differences in the coulomb coupling of D-AAs.

Through this study, we confirm that upon self-assembly of D-AAs in water, (1) a range of nanostructure geometries is achievable due to the rotational freedom of the diacetylene group, and (2) the nanostructure geometry can be chosen by varying amphiphile concentration and/or equilibration temperature. Therefore, we propose that conformational freedom might be generally integrated into the design of amphiphiles in order to fine-tune nanostructure morphologies and achieve novel supramolecular geometries from strongly interacting amphiphiles.

■ ASSOCIATED CONTENT

Supporting Information

The Supporting Information is available free of charge at https://pubs.acs.org/doi/10.1021/jacs.3c04598.

Materials, synthesis details, methods, additional TEM images, temperature dependence analysis of D-AA twisted nanoribbon morphologies, nanostructure fitting to SAXS profiles, additional UV−vis and FT-IR absorption spectra, additional CD spectra and analysis, 2D TOCSY NMR spectra, diffraction analysis of cryo-TEM images, physical appearance of nanoribbon thread by shear alignment, and additional fluorescence properties (PDF)

■ AUTHOR INFORMATION

Corresponding Author

Julia H. Ortony − *Department of Materials Science and Engineering, Massachusetts Institute of Technology, Cambridge, Massachusetts 02139, United States;* Present Address: Department of Chemistry and Biochemistry, University of California San Diego, La Jolla, CA 92093, United States.; orcid.org/0000-0001-7446-6207; Email: ortony@mit.edu

Authors

Yukio Cho − *Department of Materials Science and Engineering, Massachusetts Institute of Technology, Cambridge, Massachusetts 02139, United States;* orcid.org/0000-0003-0919-692X

Yu-Jin Choi − *Department of Materials Science and Engineering, Massachusetts Institute of Technology, Cambridge, Massachusetts 02139, United States;* Present Address: Materials Department, University of California Santa Barbara, Santa Barbara, CA 93106, United States

Samuel J. Kaser − *Department of Chemistry, Massachusetts Institute of Technology, Cambridge, Massachusetts 02139, United States;* orcid.org/0000-0002-1743-5612

Rebecca Meacham − *Department of Materials Science and Engineering, Massachusetts Institute of Technology, Cambridge, Massachusetts 02139, United States*

Ty Christoff-Tempesta − *Department of Materials Science and Engineering, Massachusetts Institute of Technology, Cambridge, Massachusetts 02139, United States;* Present Address: Department of Chemical and Biomolecular Engineering, University of Delaware, Newark, DE 19716, United States.

Siyu Wu − *X-ray Science Division, Advanced Photon Source, Argonne National Laboratory, Lemont, Illinois 60439, United States*

Xiaobing Zuo − *X-ray Science Division, Advanced Photon Source, Argonne National Laboratory, Lemont, Illinois 60439, United States*

Complete contact information is available at: https://pubs.acs.org/10.1021/jacs.3c04598

Author Contributions

Y.C. and Y-J.C. contributed equally, and the manuscript was written with contributions of all authors. All authors have given approval to the final version of the manuscript.

Funding

This material is based upon work supported by the National Science Foundation under grant number CHE-1945500. This work was supported in part by the Professor Amar G. Bose Research Grant Program. Y.C. acknowledges the support of the H.F. Taylor Fellowship. Y.-J.C. acknowledges the support of the Basic Science Research Program through the National Research Foundation of Korea (NRF) funded by the Ministry of Education (2020R1A6A3A0303738). S.K. acknowledges the support of the Natural Sciences and Engineering Research Council of Canada's postgraduate scholarship (PGS-D). R.M. acknowledges support by the National Science Foundation Graduate Research Fellowship Program under grant no. 2141064.

Notes

The authors declare no competing financial interest.

■ ACKNOWLEDGMENTS

We thank Ryan Allen for contributing graphics shown in Figure 1. We thank Edward J. Brignole and Christopher Borsa in the MIT.nano Cryo-EM Facility for their guidance on cryo-TEM sample preparation and imaging. This work made use of the MRSEC Shared Experimental Facilities at MIT supported by the National Science Foundation under award number DMR-14-19807 and the MIT Department of Chemistry Instrumentation Facility (DCIF). X-ray scattering measurements were performed at beamline 12-ID-B of the Advanced Photon Source, a US Department of Energy Office of Science User Facility operated for the US Department of Energy Office of Science by Argonne National Laboratory under contract no. DE-AC02-06CH11357. This work was performed in part on the Talos Arctica G2 Cryo-TEM, which was a gift from the Arnold and Mabel Beckman Foundation, in the MIT.nano Characterization Facilities under award number DMR-2117609.

■ REFERENCES

(1) Kushner, D. J. Self-assembly of biological structures. *Bacteriol. Rev.* **1969**, *33* (2), 302−345.

(2) Singer, S. J.; Nicolson, G. L. The Fluid Mosaic Model of the Structure of Cell Membranes. *Science* **1972**, *175* (4023), 720−731.

(3) Eisenberg, D. The discovery of the α-helix and β-sheet, the principal structural features of proteins. *Proc. Natl. Acad. Sci. U.S.A.* **2003**, *100* (20), 11207−11210.

(4) Monnard, P.-A.; Deamer, D. W. Membrane self-assembly processes: Steps toward the first cellular life. *Anat. Rec.* **2002**, *268* (3), 196−207.

(5) Aida, T.; Meijer, E. W.; Stupp, S. I. Functional Supramolecular Polymers. *Science* **2012**, *335* (6070), 813−817.

(6) Zhang, S. Fabrication of novel biomaterials through molecular self-assembly. *Nat. Biotechnol.* **2003**, *21*, 1171−1178.
(7) Webber, M. J.; Appel, E. A.; Meijer, E. W.; Langer, R. Supramolecular biomaterials. *Nat. Mater.* **2016**, *15*, 13−26.
(8) Hartgerink, J. D.; Beniash, E.; Stupp, S. I. Self-Assembly and Mineralization of Peptide-Amphiphile Nanofibers. *Science* **2001**, *294* (5547), 1684−1688.
(9) Ortony, J. H.; Newcomb, C. J.; Matson, J. B.; Palmer, L. C.; Doan, P. E.; Hoffman, B. M.; Stupp, S. I. Internal dynamics of a supramolecular nanofibre. *Nat. Mater.* **2014**, *13*, 812−816.
(10) Weingarten, A. S.; Kazantsev, R. V.; Palmer, L. C.; McClendon, M.; Koltonow, A. R.; Samuel, A. P. S.; Kiebala, D. J.; Wasielewski, M. R.; Stupp, S. I. Self-assembling hydrogel scaffolds for photocatalytic hydrogen production. *Nat. Chem.* **2014**, *6* (11), 964−970.
(11) Das, A.; Ghosh, S. Supramolecular assemblies by charge-transfer interactions between donor and acceptor chromophores. *Angew. Chem., Int. Ed.* **2014**, *53* (8), 2038−2054.
(12) Schnur, J. M. Lipid Tubules: A paradigm for molecularly engineered structures. *Science* **1993**, *262* (5140), 1669−1676.
(13) Fuhrhop, J. H.; Helfrich, W. Fluid and solid fibers made of lipid molecular bilayers. *Chem. Rev.* **1993**, *93* (4), 1565−1582.
(14) Christoff-Tempesta, T.; Cho, Y.; Kim, D.-Y.; Geri, M.; Lamour, G.; Lew, A. J.; Zuo, X.; Lindemann, W. R.; Ortony, J. H. Self-assembly of aramid amphiphiles into ultra-stable nanoribbons and aligned nanoribbon threads. *Nat. Nanotechnol.* **2021**, *16* (4), 447−454.
(15) Cho, Y.; Christoff-Tempesta, T.; Kaser, S. J.; Ortony, J. H. Dynamics in supramolecular nanomaterials. *Soft Matter* **2021**, *17* (24), 5850−5863.
(16) Whitesides, G. M.; Grzybowski, B. Self-assembly at all scales. *Science* **2002**, *295* (5564), 2418−2421.
(17) Stupp, S. I.; Zha, R. H.; Palmer, L. C.; Cui, H.; Bitton, R. Self-assembly of biomolecular soft matter. *Faraday Discuss.* **2013**, *166*, 9−30.
(18) Dumele, O.; Chen, J.; Passarelli, J. V.; Stupp, S. I. Supramolecular energy materials. *Adv. Mater.* **2020**, *32* (17), 1907247.
(19) Gelain, F.; Luo, Z.; Rioult, M.; Zhang, S. Self-assembling peptide scaffolds in the clinic. *npj Regener. Med.* **2021**, *6* (1), 9.
(20) Mitchell, M. J.; Billingsley, M. M.; Haley, R. M.; Wechsler, M. E.; Peppas, N. A.; Langer, R. Engineering precision nanoparticles for drug delivery. *Nat. Rev. Drug Discovery* **2021**, *20* (2), 101−124.
(21) Shimizu, T.; Ding, W.; Kameta, N. Soft-Matter Nanotubes: A Platform for Diverse Functions and Applications. *Chem. Rev.* **2020**, *120* (4), 2347−2407.
(22) Cho, Y.; Christoff-Tempesta, T.; Kim, D.-Y.; Lamour, G.; Ortony, J. H. Domain-selective thermal decomposition within supramolecular nanoribbons. *Nat. Commun.* **2021**, *12* (1), 7340.
(23) Tao, K.; Makam, P.; Aizen, R.; Gazit, E. Self-assembling peptide semiconductors. *Science* **2017**, *358* (6365), No. eaam9756.
(24) Lee, J.-H.; Heo, K.; Schulz-Schönhagen, K.; Lee, J. H.; Desai, M. S.; Jin, H.-E.; Lee, S.-W. Diphenylalanine Peptide Nanotube Energy Harvesters. *ACS Nano* **2018**, *12* (8), 8138−8144.
(25) Gilboa, B.; Lafargue, C.; Handelman, A.; Shimon, L. J. W.; Rosenman, G.; Zyss, J.; Ellenbogen, T. Strong Electro-Optic Effect and Spontaneous Domain Formation in Self-Assembled Peptide Structures. *Advanced Science* **2017**, *4* (9), 1700052.
(26) Maity, S. K.; Kumar, R.; Ambast, D. K. S.; Pal, B.; Haldar, D. Self-assembly and nonlinear optical properties of a synthetic dipeptide. *J. Mater. Chem.* **2012**, *22* (41), 22198−22203.
(27) Choi, Y.-J.; Park, S.; Yoon, W.-J.; Lim, S.-I.; Koo, J.; Kang, D.-G.; Park, S.; Kim, N.; Jeong, K.-U. Imidazolium-Functionalized Diacetylene Amphiphiles: Strike a Lighter and Wear Polaroid Glasses to Decipher the Secret Code. *Adv. Mater.* **2020**, *32* (39), 2003980.
(28) Christoff-Tempesta, T.; Ortony, J. H. Emerging investigator series: aramid amphiphile nanoribbons for the remediation of lead from contaminated water. *Environ. Sci.: Nano* **2021**, *8* (6), 1536−1542.
(29) Stupp, S. I.; Palmer, L. C. Supramolecular Chemistry and Self-Assembly in Organic Materials Design. *Chem. Mater.* **2014**, *26* (1), 507−518.
(30) Kim, D.-Y.; Christoff-Tempesta, T.; Lamour, G.; Zuo, X.; Ryu, K.-H.; Ortony, J. H. Morphological Transitions of a Photoswitchable Aramid Amphiphile Nanostructure. *Nano Lett.* **2021**, *21* (7), 2912−2918.
(31) Kaser, S. J.; Lew, A. J.; Kim, D.-Y.; Christoff-Tempesta, T.; Cho, Y.; Ortony, J. H. Effects of molecular flexibility and head group repulsion on aramid amphiphile self-assembly. *Mol. Syst. Des. Eng.* **2021**, *6* (12), 1016−1024.
(32) Xiong, Q.; Jiang, Y.; Cai, X.; Yang, F.; Li, Z.; Han, W. Conformation Dependence of Diphenylalanine Self-Assembly Structures and Dynamics: Insights from Hybrid-Resolution Simulations. *ACS Nano* **2019**, *13* (4), 4455−4468.
(33) Zhu, M.; Zhu, L. Rational Design of Diphenyldiacetylene-Based Fluorescent Materials Enabling a 365-nm Light-Initiated Topochemical Polymerization. *Chem.—Asian J.* **2021**, *16* (15), 2048−2054.
(34) Sangji, M. H.; Sai, H.; Chin, S. M.; Lee, S. R.; R Sasselli, I.; Palmer, L. C.; Stupp, S. I. Supramolecular Interactions and Morphology of Self-Assembling Peptide Amphiphile Nanostructures. *Nano Lett.* **2021**, *21* (14), 6146−6155.
(35) Mertens, H. D. T.; Svergun, D. I. Structural characterization of proteins and complexes using small-angle X-ray solution scattering. *J. Struct. Biol.* **2010**, *172* (1), 128−141.
(36) Nallet, F.; Laversanne, R.; Roux, D. Modelling X-ray or neutron scattering spectra of lyotropic lamellar phases: interplay between form and structure factors. *J. Phys. II* **1993**, *3* (4), 487−502.
(37) Wehner, M.; Röhr, M. I. S.; Bühler, M.; Stepanenko, V.; Wagner, W.; Würthner, F. Supramolecular Polymorphism in One-Dimensional Self-Assembly by Kinetic Pathway Control. *J. Am. Chem. Soc.* **2019**, *141* (14), 6092−6107.
(38) Grabicki, N.; Dumele, O.; Sai, H.; Powers-Riggs, N. E.; Phelan, B. T.; Sangji, M. H.; Chapman, C. T.; Passarelli, J. V.; Dannenhoffer, A. J.; Wasielewski, M. R.; Stupp, S. I. Polymorphism and Optoelectronic Properties in Crystalline Supramolecular Polymers. *Chem. Mater.* **2021**, *33* (2), 706−718.
(39) Kaser, S. J.; Christoff-Tempesta, T.; Uliassi, L. D.; Cho, Y.; Ortony, J. H. Domain-Specific Phase Transitions in a Supramolecular Nanostructure. *J. Am. Chem. Soc.* **2022**, *144* (39), 17841−17847.
(40) Abbel, R.; Schleuss, T. W.; Frey, H.; Kilbinger, A. F. M. Rod-Length Dependent Aggregation in a Series of Oligo(p-benzamide)-Block-Poly(ethylene glycol) Rod-Coil Copolymers. *Macromol. Chem. Phys.* **2005**, *206* (20), 2067−2074.
(41) Baranović, G.; Colombo, L.; Furić, K.; Durig, J. R.; Sullivan, J. F.; Mink, J. Vibrational assignment of 1,4-diphenylbutadiyne. *J. Mol. Struct.* **1986**, *144* (1−2), 53−69.
(42) Sebree, J. A.; Zwier, T. S. The excited states and vibronic spectroscopy of diphenyldiacetylene and diphenylvinylacetylene. *Phys. Chem. Chem. Phys.* **2012**, *14* (1), 173−183.
(43) Feng, W.; Kim, J.-Y.; Wang, X.; Calcaterra, H. A.; Qu, Z.; Meshi, L.; Kotov, N. A. Assembly of mesoscale helices with near-unity enantiomeric excess and light-matter interactions for chiral semiconductors. *Sci. Adv.* **2017**, *3* (3), No. e1601159.
(44) Song, M.; Tong, L.; Liu, S.; Zhang, Y.; Dong, J.; Ji, Y.; Guo, Y.; Wu, X.; Zhang, X.; Wang, R.-Y. Nonlinear Amplification of Chirality in Self-Assembled Plasmonic Nanostructures. *ACS Nano* **2021**, *15* (3), 5715−5724.
(45) Wolffs, M.; George, S. J.; Tomović, Ž.; Meskers, S. C. J.; Schenning, A. P. H. J.; Meijer, E. W. Macroscopic Origin of Circular Dichroism Effects by Alignment of Self-Assembled Fibers in Solution. *Angew. Chem., Int. Ed.* **2007**, *46* (43), 8203−8205.
(46) Anuradha; La, D. D.; Al Kobaisi, M.; Bhosale, S. V. Right handed chiral superstructures from achiral molecules: self-assembly with a twist. *Sci. Rep.* **2015**, *5* (1), 15652.
(47) Nadimetla, D. N.; Al Kobaisi, M.; Bugde, S. T.; Bhosale, S. V. Tuning Achiral to Chiral Supramolecular Helical Superstructures. *Chem. Rec.* **2020**, *20* (8), 793−819.
(48) Choi, Y.-J.; Jung, D.; Lim, S.-I.; Yoon, W.-J.; Kim, D.-Y.; Jeong, K.-U. Diacetylene-Functionalized Dendrons: Self-Assembled and Photopolymerized Three-Dimensional Networks for Advanced Self-

Healing and Wringing Soft Materials. *ACS Appl. Mater. Interfaces* **2020**, *12* (29), 33239−33245.
(49) Herkert, L.; Droste, J.; Kartha, K. K.; Korevaar, P. A.; de Greef, T. F. A.; Hansen, M. R.; Fernández, G. Pathway Control in Cooperative vs. Anti-Cooperative Supramolecular Polymers. *Angew. Chem., Int. Ed.* **2019**, *58* (33), 11344−11349.
(50) Hestand, N. J.; Spano, F. C. Expanded Theory of H- and J-Molecular Aggregates: The Effects of Vibronic Coupling and Intermolecular Charge Transfer. *Chem. Rev.* **2018**, *118* (15), 7069−7163.
(51) Bricks, J. L.; Slominskii, Y. L.; Panas, I. D.; Demchenko, A. P. Fluorescent J-aggregates of cyanine dyes: basic research and applications review. *Methods Appl. Fluoresc.* **2017**, *6* (1), 012001.
(52) Thulstrup, P. W.; Hoffmann, S. V.; Hansen, B. K. V.; Spanget-Larsen, J. Unique interplay between electronic states and dihedral angle for the molecular rotor diphenyldiacetylene. *Phys. Chem. Chem. Phys.* **2011**, *13* (36), 16168−16174.
(53) Bradley, D.; Branley, C. P.; Peeks, M. D. A straightforward method to quantify the electron-delocalizing ability of π-conjugated molecules. *Phys. Chem. Chem. Phys.* **2022**, *24* (19), 11486−11490.
(54) Pati, A. K.; Gharpure, S. J.; Mishra, A. K. Substituted diphenyl butadiynes: a computational study of geometries and electronic transitions using DFT/TD-DFT. *Phys. Chem. Chem. Phys.* **2014**, *16* (27), 14015−14028.
(55) Wierzbicka, M.; Bylińska, I.; Sikorski, A.; Czaplewski, C.; Wiczk, W. Experimental and theoretical studies of spectroscopic properties of simple symmetrically substituted diphenylbuta-1,3-diyne derivatives. *Photochem. Photobiol. Sci.* **2015**, *14* (12), 2251−2260.
(56) Chen, G.; Li, W.; Zhou, T.; Peng, Q.; Zhai, D.; Li, H.; Yuan, W. Z.; Zhang, Y.; Tang, B. Z. Conjugation-Induced Rigidity in Twisting Molecules: Filling the Gap Between Aggregation-Caused Quenching and Aggregation-Induced Emission. *Adv. Mater.* **2015**, *27* (30), 4496−4501.

https://doi.org/10.1021/jacs.3c04598
J. Am. Chem. Soc. 2023, 145, 22954−22963